Journal of Mechanical Science and Technology 30 (8) (2016) 3641~3650
www.springerlink.com/content/1738-494x(Print)/1976-3824(Online)
DOI 10.1007/s12206-016-0725-1

# Analysis of vorticity dynamics for hump characteristics of a pump turbine model [†]

Deyou Li[1], Ruzhi Gong[1], Hongjie Wang[1,*], Lei Han[1], Xianzhu Wei[1,2] and Daqing Qin[1,2]

[1]*School of Energy Science and Engineering, Harbin Institute of Technology, Harbin 150001, China*
[2]*State Key Laboratory of Hydro-Power Equipment, Harbin Institute of Large Electrical Machinery, Harbin 150040, China*

(Manuscript Received October 12, 2015; Revised March 29, 2016; Accepted April 19, 2016)

---

## Abstract

Conventional parameters based on CFD methodology for the investigation on hump characteristics of a pump turbine cannot reflect the dynamic interaction mechanism between the runner and the fluid. This research presents a dynamic interaction mechanism of a pump turbine operating in the hump region. First, vorticity dynamic parameters were obtained based on the theory of vorticity dynamics. Second, 3-D unsteady flow simulations were performed in a full pump turbine model using the SST $k$-$\omega$ turbulence model, and numerical results have a good agreement with the experiments. Then, analysis was carried out to determine the relation between the vorticity dynamic parameters and hump characteristics. The results indicate that the theory of vorticity dynamics has an advantage in evaluating the dynamic performance of a pump turbine. The energy transfer between the runner and the fluid is through vorticity dynamic parameters-pressure and friction terms, in which the pressure term accounts for the most. Furthermore, vortex generation mainly results from the skin friction. Combining vorticity dynamic analysis with the method of Q-criterion indicates that hump characteristics are related to the reduction of the surface normal pressure work and vortex motion on the suction surfaces close to the leading edges in the runner, and the increase of skin friction work in the stay-guide vanes.

*Keywords*: Pump turbine; Pump mode; Hump characteristics; Vortex motion; Vorticity dynamics

---

## 1. Introduction

Pumped storage power plants have grown rapidly for supplying energy storage and meeting the demand for upgrading the electricity grid. In fact, pump turbines switch frequently between the pump and turbine modes to meet any changes of the supply and the demand, so they will usually operate at off-design conditions. One feature of unstable behaviors in pump mode of a pump turbine is well known. It shows a drop in head in pump mode as the discharge is reduced. There usually appears a hump region in the head-discharge curve [1]. During this hump region, the flow becomes unstable and the vibration increases obviously. The hump characteristics will harm the whole unit and prolong the start time during the starting period. The mechanism of hump characteristics is still unclear. For investigation of the instability of pump-turbines, a great amount of research has been carried out. Braun [2] analyzed the flow phenomena related to the unstable energy-discharge characteristics, concluding that a sudden change in the global performance parameters is related to a change of the secondary flow pattern in the diffuser channels. However, this conclusion was based on a single channel simulation without consideration of the interaction between the guide vanes. Liu et al. [3] predicted a better hump characteristic curve using an improved cavitation model. The analysis shows that hump characteristics might be attributed to the appearance of cavitation at the suction surfaces of the runner inlet. Yang et al. [4] carried out an experimental investigation at the hump instability region in a two-stage reversible pump turbine. The results indicate that unsteady perturbation in the instability region is coupled with an unsteady 3D pattern into the diffuser vane channels. Ran et al. [5] did experiments on pressure fluctuation in the hump region; 0.2 times the impeller rotational frequency was measured in this unsteady region, which is believed to be induced by the rotating stall in the flow passages of the wicket gates. In addition, the results show the hump characteristics experience a hysteresis phenomenon. There are also some new strategies for hydraulic machinery. Yan et al. [6] investigated the influence of water compressibility on pressure fluctuation by rotor stator interaction in a pump turbine. Gong et al. [7] applied entropy theory for analyzing the hydraulic loss. The method of entropy production analysis has the advantage of determining the quantity of energy dissipation and where the dissipation happens. Li et al. [8] conducted dynamic analysis on pressure fluctuation in the vaneless region of a pump turbine model using a dynamic mesh method in turbine mode. It can be concluded that pressure fluctuation

---

[*] Corresponding author. Tel.: +86 13903610856, Fax.: +86 4513254
E-mail address: wanghongjie@hit.edu.cn; lideyou@hit.edu.cn

[†] Recommended by Associate Editor Jun Sang Park

in the vaneless region is strongly influenced by the oscillating of the guide vanes. Additionally, they [9] performed unsteady simulations in pump mode of a pump-turbine and concluded that the vortex movement is related with hump characteristics at partial discharge operating conditions.

All the above studies focus on the relation between the hump characteristics and unsteady patterns. How and where the unsteady patterns are generated is still unclear. However, conventional parameters based on CFD methodology for investigating hump characteristics in a pump turbine cannot reflect the dynamic interaction mechanism between the runner and the fluid [10]. Based on the research method proposed by Wu in the middle of 1980s, Wu et al. [11] set up a complete vorticity dynamics theory. They explored the pneumatic diagnosis method based on local vorticity dynamics, and successfully applied on the aerodynamic optimization design. Then, a number of researchers studied this vorticity dynamics and achieved some results [12-14]. To analyze the dynamic interaction mechanism between the runner and the fluid of hydraulic turbines, vorticity dynamics theory was introduced. Li et al. [15] applied it for design and optimization for runner blades of a tubular turbine. Zhang et al. [16] analyzed flow characteristics in a Francis hydraulic turbine based on this theory. It could reflect the dynamic interaction mechanism inside the runner, directly show energy transfer between the blades and the fluid, and find the defects of the designed runner for improving the performance of design and actual operation.

However, this theory has not yet been applied to pump turbines, especially for hump characteristics analysis. Hence, this paper presents a dynamic interaction mechanism between the rotating runner and the fluid of a pump turbine operating in the hump region based on the theory of vorticity dynamics.

## 2. Vorticity dynamics theory

For Newtonian fluids, the Navier-Stokes momentum equation is shown as follows:

$$\frac{\mathrm{D}\vec{v}}{\mathrm{D}t} = \vec{f} - \frac{1}{\rho}\nabla p + \frac{1}{3}\mu\nabla(\nabla\cdot\vec{v}) + \mu\nabla^2\vec{v} , \tag{1}$$

where $\vec{v}$ is flow velocity. $\rho$, $p$ and $\mu$ are density, pressure, and dynamic viscosity of the fluid, respectively. $\vec{f}$ stands for a conservative external body force.

With the idea of the vorticity field $\vec{\omega}$, it is defined as $\vec{\omega} = \nabla\times\rho\vec{v}$ . Vorticity is a kinematic property of the flow field which, at each point, measures the angular velocity of a fluid particle. It is a vector quantity, having three scalar components. In fact, the vorticity field is like a magnetic field in that it has zero divergence ( $\nabla\cdot\vec{\omega} = 0$ ).

Taking the curl of each term in Eq. (1) and re-arranging the result, where $\nabla\cdot\vec{\omega} = 0$ , one obtains [19]

$$\begin{aligned}&\frac{\partial\vec{\omega}}{\partial t} + (\vec{\omega}\times\nabla)\vec{v} - \vec{\omega}(\nabla\times\vec{v}) = (\vec{\omega}\cdot\nabla)\vec{v} - \vec{\omega}(\nabla\cdot\vec{v})\\ &+\nabla\times\rho\vec{f} - \nabla\times(\nabla p) + \mu\rho\nabla^2\vec{\omega} .\end{aligned} \tag{2}$$

Eq. (2), the vorticity transport equation, describes the change of the vorticity field with time. The first term on the right hand side of Eq. (2) represents the vortex line stretching and bending caused by the velocity gradient effect, thus changing magnitude and direction of the vorticity. The second term represents the change of vorticity magnitude with the volume of the fluid. The third term is related to the contribution of body force. The fourth term is zero in a barotropic fluid and the last term is the effect caused by viscous dissipation.

Generally, the fluid is considered as a barotropic fluid and the body force is negligible, thus Eq. (2) yields

$$\frac{\partial\vec{\omega}}{\partial t} + (\vec{\omega}\times\nabla)\vec{v} - \vec{\omega}(\nabla\times\vec{v}) = (\vec{\omega}\cdot\nabla)\vec{v} - \vec{\omega}(\nabla\cdot\vec{v}) + \mu\rho\nabla^2\vec{\omega} . \tag{3}$$

For any vector $\vec{b}$ related to its position in three dimensions [18], one has

$$\int_{V_f}\vec{b}d\tau = \frac{1}{N-1}\int_{V_f}\vec{r}\times(\vec{\nabla}\times\vec{b})d\tau - \frac{1}{N-1}\int_{S}\vec{r}\times(\vec{n}\times\vec{b})ds , \tag{4}$$

where $\vec{b}$ stands for any vector specified, N is related to the dimension; $N$ is 3 when it is 3-D (three dimensions) or 2 when it is 2-D (two dimensions). $V_f$ represents the control volume and $S$ is the control surface. $\vec{n}$ is the normal direction of the control surface.

Letting $\rho\vec{v} = \vec{b}$ , Eq. (4) can be expressed as

$$\int_{V_f}\rho\vec{v}d\tau = \int_{V_f}\frac{1}{M}\vec{r}\times(\nabla\times\rho\vec{v})d\tau - \int_{S}\frac{1}{M}\vec{r}\times(\vec{n}\times\rho\vec{v})ds , \tag{5}$$

$$\rho\vec{v} = \frac{1}{M}(\vec{r}\times\vec{\omega}) + \frac{1}{M}\nabla\cdot(\vec{r}\cdot(\rho\vec{v})I) - \frac{1}{M}\nabla(\vec{r}\cdot(\rho\vec{v})) , \tag{6}$$

where $M = N-1$ , and $I$ is a second-order tensor. Taking the first moment of $\rho\vec{v}$ ,

$$\vec{r}\times\rho\vec{v} = -\frac{1}{M}\vec{r}^2\vec{\omega} + \frac{1}{M}\nabla\times(r^2\cdot\rho\vec{v}) . \tag{7}$$

If a system contains solid and fluid, one can get a new fluid system composed of the solid surface and fluid around the surface. According to the momentum theorem, the total force is equal to the time rate of the total momentum of the fluid system:

$$-\vec{F} = \frac{D}{Dt}\int_{V_f}\rho\vec{v}d\tau . \tag{8}$$

Using Eq. (6), one obtains from Eq. (8):

$$\vec{F} = -\frac{1}{M}\frac{D}{Dt}\left(\int_{V_f}(\vec{r}\times\vec{\omega})d\tau + \int_{\sum_f}\vec{r}\times(\vec{n}\times\rho\vec{v})ds\right) . \tag{9}$$

Meanwhile, according to the theorem of momentum moment, the total moment is equal to the time rate of the total momentum moment of the fluid system [18]:

$$\vec{M} = -\frac{D}{Dt}\int_{V_f}(\vec{r}\times\rho\vec{v})d\tau \,. \tag{10}$$

Using Eq. (7), one obtains from Eq. (10):

$$\vec{M} = \frac{1}{M}\frac{D}{Dt}\int_{V_f} r^2\vec{\omega}d\tau - \frac{1}{M}\frac{D}{Dt}\int_{\Sigma_f} r^2\left(\vec{n}\times\left(\rho\vec{v}\right)\right)ds \,. \tag{11}$$

In Eqs. (9) and (11), $\int_{V_f}\left(\vec{r}\times\vec{\omega}\right)d\tau$ and $\int_{V_f} r^2\vec{\omega}d\tau$, respectively, stand for the total first and the second moment of the vorticity in the control volume $V_f$.

Using Eq. (3), the time rate of the total first moment of vorticity can be given as following:

$$\begin{aligned}&\frac{1}{M}\int_{V_f}\vec{r}\times\frac{\partial\vec{\omega}}{\partial t}d\tau = \frac{1}{M}\int_{V_f}\vec{r}\times\left[\nabla\times\left(\vec{v}\times\vec{\omega}\right)\right]d\tau - \\ &\frac{1}{M}\mu\int_{V_f}\vec{r}\times\left[\nabla\times\left(\nabla\times\vec{\omega}\right)\right]d\tau \,.\end{aligned} \tag{12}$$

The first term on the right hand of Eq. (12):

$$\begin{aligned}&\frac{1}{M}\int_{V_f}\vec{r}\times\left[\nabla\times\left(\vec{v}\times\vec{\omega}\right)\right]d\tau = \int_{V_f}\vec{v}\times\vec{\omega}d\tau + \\ &\frac{1}{M}\int_{\Sigma_f}\vec{r}\times(\vec{n}\times(\vec{v}\times\vec{\omega}))ds \,.\end{aligned} \tag{13}$$

The second term on the right hand of the Eq. (12):

$$\begin{aligned}&-\frac{1}{\mathrm{M}}\mu\int_{V_f}\vec{r}\times\left[\nabla\times\left(\nabla\times\vec{\omega}\right)\right]d\tau = -\mu\int_{V_f}\nabla\times\vec{\omega}d\tau + \\ &\frac{\mu}{\mathrm{M}}\int_{\Sigma_f}\vec{r}\times(\vec{n}\times(\nabla\times\vec{\omega}))ds \,.\end{aligned} \tag{14}$$

Then we define $\vec{b} = \nabla\times\vec{\omega}$ in Eq. (4). Combining Eqs. (9), (13) and (14), we get the total force as follows:

$$\begin{aligned}\vec{F} &= \int_{V_f}\vec{v}\times\vec{\omega}d\tau + \frac{1}{M}\int_{\Sigma_f}\vec{r}\times\left(\vec{n}\times\left(\vec{v}\times\vec{\omega}\right)\right)ds - \mu\int_{V_f}\nabla\times\vec{\omega}dv \\ &-\frac{\mu}{M}\int_{\Sigma_f}\vec{r}\times\left(\vec{n}\times\left(\nabla\times\vec{\omega}\right)\right)ds + \int_{\Sigma_f}\vec{r}\times\left(\vec{n}\times\rho\vec{v}\right)ds \,.\end{aligned} \tag{15}$$

For a pump turbine, the fluid system is the runner blade and the fluid inside it. $\vec{v}$ is relative velocity of the blade surface and its value is zero due to no-slip condition and constant rotational speed. The volume integral is converted to surface integral for the first term on the right hand side of Eq. (15) using Gauss theorem. Therefore, the total force acting on the fluid could be re-arranged below:

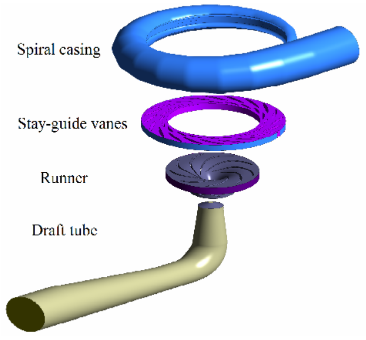

Fig. 1. Computational domain of the pump turbine model.

$$\vec{F} = \int_{\Sigma_f}\mu(\vec{n}\times\vec{\omega})ds - \frac{\mu}{M}\int_{\Sigma_f}\vec{r}\times\left(\vec{n}\times\left(\nabla\times\vec{\omega}\right)\right)ds \,. \tag{16}$$

Then, using the same process as the total force acting, we get the total moment acting on the fluid:

$$\vec{M} = \int_{\Sigma_f}\mu\vec{r}\times(\vec{n}\times\vec{\omega})ds - \frac{\mu}{M}\int_{\Sigma_f} r^2\vec{n}\times(\nabla\times\vec{\omega})ds \,. \tag{17}$$

Then, we define four vorticity parameters from the total force and moment in Eqs. (16) and (17):

$$vor_1 = \mu(\vec{n}\times\vec{\omega}) \,, \tag{18}$$

$$vor_2 = \mu\vec{r}\times(\vec{n}\times(\nabla\times\vec{\omega})) \,, \tag{19}$$

$$vor_3 = \mu\vec{r}\times(\vec{n}\times\vec{\omega}) \,, \tag{20}$$

$$vor_4 = \mu r^2\vec{n}\times(\nabla\times\vec{\omega}) \,. \tag{21}$$

In Eqs. (18)-(21), $vor_1$ refers to skin friction, $vor_2$ refers to surface normal pressure, then $vor_3$ and $vor_4$ are the skin friction work and the surface normal pressure work, respectively, corresponding to $vor_1$ and $vor_2$. From Eq. (17), it can be concluded that the energy transfer between the runner and the fluid is through vorticity dynamic parameters-pressure (surface normal pressure) and friction terms (skin friction). In the post processing, these four parameters were obtained through the method of user-defined variables. Vorticity in the different directions could be obtained using the parameters of the velocity from the numerical results. Then, we get the vorticity dynamic parameters through the cross-product of the vorticity and the rest of the parameters are known in the numerical simulations.

## 3. Numerical model and scheme setup

### 3.1 Computational domain

The computational domain includes the whole reduced scale reversible pump turbine model, from the draft tube inlet to the spiral casing outlet as shown in Fig. 1. The whole model is composed of four main components as follows: Spiral cas-

Table 1. Parameters of the pump turbine model (Pump mode).

| Parameters | Values |
|---|---|
| Diameter of runner outlet (mm) | 524 |
| Diameter of runner inlet (mm) | 274 |
| Number of runner blades | 9 |
| Number of stay vanes | 20 |
| Height of guide vanes (mm) | 45.77 |
| Number of guide vanes | 20 |
| Specific speed ($\text{min}^{-1}$) | 30.7 |

ing, stay-guide vanes, runner and draft tube. Table 1 gives the parameters of the reduced scale reversible pump turbine. The specific speed stands for the speed of an ideal pump geometrically similar to the actual pump, which when running at this speed will raise a unit of volume, in a unit of time through a unit of head.

### 3.2 Numerical scheme

ANSYS CFX 14.0 commercial code was used to do the unsteady incompressible turbulent flow numerical simulations, while the finite volume method was used to solve both the incompressible unsteady Reynolds-averaged Navier-Stokes equations in their conservative form and the mass conservation equations. In the CFX, a large number of turbulence models are available. Among them, the SST $k$-$\omega$ turbulence model combines the advantages of $k$-$\omega$ and $k$-$\varepsilon$. In the boundary layer, it can be used as a low-Reynolds number turbulence model without any extra damping functions. In the free-stream, it can switch to a $k$-$\varepsilon$ behavior to avoid the common problem that is too sensitive to the inlet free-stream turbulence properties. Moreover, it shows good prediction in adverse pressure gradient and separating flows. With respect to the flow in the pump mode of a pump turbine, serious separation exists in the runner and stay-guide vane channels, especially at off-design conditions. Furthermore, we have compared four turbulence models (SST $k$-$\omega$, standard $k$-$\omega$, RNG $k$-$\varepsilon$ and standard $k$-$\varepsilon$) using the same pump-turbine as in the previously published paper [20]. The results show all of these four turbulence models show good results around the BEP, while SST $k$-$\omega$ show better results at partial discharge conditions. Hence, in this research, the two-equation SST $k$-$\omega$ turbulence model was chosen to close the URANS equations. The high resolution scheme for advection term and the 2nd order upwind scheme for other terms was used. Finally, a time step corresponding to 1 degree of the runner revolution and a convergence criterion $\text{RMS}_{\text{max}}<10^{-6}$ with ten internal coefficient loops were selected. An interface strategy was employed to connect topologically non-matched mesh regions. For transient simulations, the frame change interfaces based on the General grid interface (GGI) were set as transient rotor stator, which can greatly change the orientation of the non-matched rotating, and stationary domains at each time step.

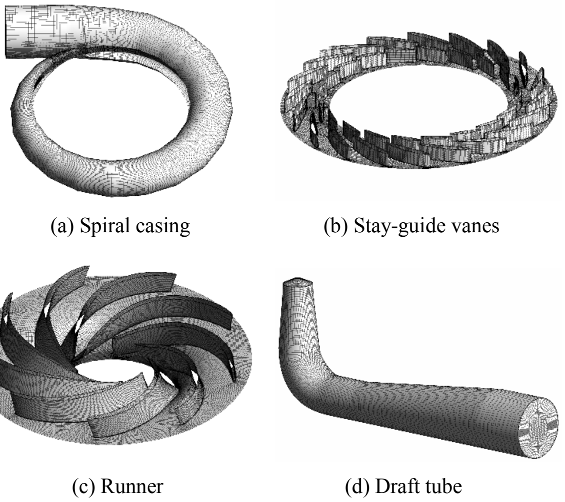
(a) Spiral casing (b) Stay-guide vanes

(c) Runner (d) Draft tube

Fig. 2. Grids for different components.

### 3.3 Boundary conditions

Discharge at the draft tube inlet was specified in pump mode according to the experiments. Additionally, intensity and auto compute length was selected for the turbulence term, and the fractional intensity was specified as 0.02. At the spiral casing outlet, static pressure (0 Pa) was set. No-slip wall conditions for all the solid walls were imposed. An automatic near-wall treatment method was applied for the SST $k$-$\omega$ turbulence model, which allows a gradual switch between wall functions and low-Reynolds number grids, without a loss in accuracy.

### 3.4 Grid sensitivity test

Grids for different parts (spiral casing, stay-guide vanes, runner and draft tube) are shown in Fig. 2. To meet the requirements of the chosen turbulence model (SST $k$-$\omega$), the mesh layers off the wall are more than 10. $y^+$ at wall layer of the runner and stay-guide vanes is less than 11. $y^+$ in average for these two parts is less than 2 (see Table 2). The size of the grids or the total number of the nodes is of great importance for the calculation accuracy. The grid sensitivity was verified at the Best efficiency point (BEP) under 19 mm guide vane opening. Structured grids were generated in each flow passage except the tongue of the spiral casing. Due to sharp shape of tongue, an unstructured grid was created for this part. The total number of nodes increases from $1.2\times10^6$ to $9.2\times10^6$. 3-D unsteady flow numerical simulations were carried out to calculate the head and hydraulic efficiency under different conditions. It is evident from Fig. 3 that the head and hydraulic efficiency change little if the grid number is larger than $7.9\times10^6$. Considering the numerical accuracy and the cost of computational resources, the number $7.9\times10^6$ was employed in the following simulations. Detailed information for different parts is listed in Table 2.

Table 2. Grid information for different components.

| Part | Quality | $y+$ | Nodes (million) | |
|---|---|---|---|---|
| Spiral casing | 0.48 | 300 | 0.48 | Structured |
| Tongue | 0.31 | | | Unstructured |
| Runner | 0.61 | 1.141 | 3.89 | 18 layers<br>The distance of first layer<br>0.003 mm |
| Stay-guide vanes | 0.5 | 1.909 | 3.10 | Structured |
| Draft tube | 0.63 | 7.34 | 0.45 | Structured |
| Total | | | 7.92 | Structured |

Table 3. Characteristics of the test rig.

| Characteristic | Value |
|---|---|
| Maximum head [m] | 80 |
| Maximum discharge [$m^3/s$] | 0.8 |
| Runner diameter range [mm] | 300~500 |
| Generating power [kW] | 750 |
| The test rig accuracy for all the parameters | ±0.20% |

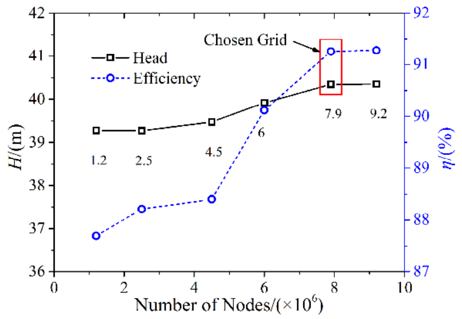

Fig. 3. Grid sensitivity validation (head, efficiency).

Fig. 4. The investigated pump-turbine model installed in the test rig.

### 3.5 Experimental validation

The pump turbine model was installed in a test rig of Harbin Institute of Large Electric Machinery (see Fig. 4). Main parameters are listed in Table 3. The test rig allows for both turbine and pump performance assessment within an accuracy of 0.2%, meeting the IEC standards [21].

Table 4. Chosen operating points for analysis.

| Points | $Q_m$ ($kg{\cdot}s^{-1}$) | $\eta_{Num}$ (%) | $\eta_{Exp}$ (%) |
|---|---|---|---|
| $1.34Q_{BEP}$ | 301.50 | 88.38 | 87.51 |
| $1.00Q_{BEP}$ | 224.36 | 92.122 | 90.69 |
| $0.72Q_{BEP}$ | 160.96 | 84.76 | 82.37 |
| $0.56Q_{BEP}$ | 126.62 | 79.17 | 74.27 |

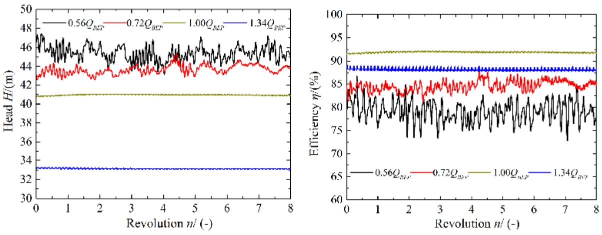

(a) Head (b) Efficiency

Fig. 5. Computational results of the rest of the eight revolutions.

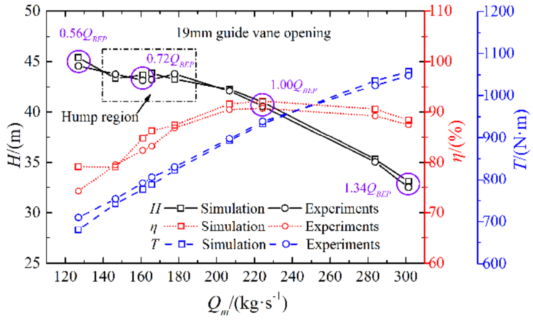

Fig. 6. Performance curves at 19 mm guide vane opening.

The internal flow field of the pump turbine is complex in pump mode, and could not be easily observed through experimental facilities. Therefore, several operating points were calculated at 19 mm guide vane opening according to the performance curve. In this research, all the unsteady simulations were calculated for 15 revolutions; the first seven revolutions were deleted to avoid the unstable data. The results of the rest of the eight revolutions were averaged to obtain the values of the head, torque and efficiency. The monitoring values for head and efficiency are shown in Fig. 5. As for $1.00Q_{BEP}$ and $1.34Q_{BEP}$, the variation of the head and torque shows small over the eight revolutions. However, the fluctuations of head and torque increase obviously as the discharge is reduced. The performance curves are shown in Fig. 6.

The head in the head-discharge curve of 19 mm guide vane opening shows an obvious decline at large partial flow conditions. From Fig. 6, the calculation errors for the head in whole range show relatively small (less than 2%). The maximum error (1.94%) occurs in the large discharge operating point. The errors for small discharge and hump region points show a bit larger in the complete operating range, which are 1.84% and 1.45%, respectively. The errors for the rest operating points are all less than 1%. Information on the chosen operating points marked in Fig. 6 for analysis is given in Table 4. As

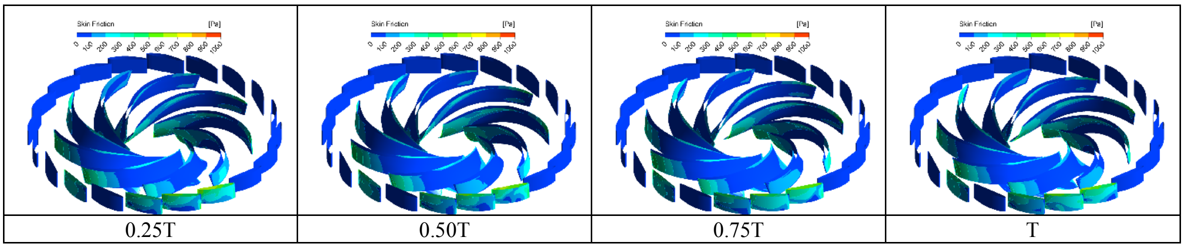

0.25T | 0.50T | 0.75T | T

Fig. 7. The distribution of skin friction over one period.

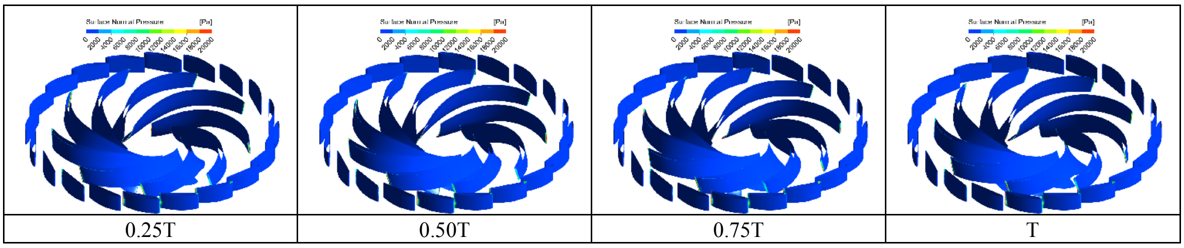

0.25T | 0.50T | 0.75T | T

Fig. 8. The distribution of surface normal pressure over one period.

for torque-discharge curve, the torque decreases with reduction of the discharge, and relative errors for most operating points are less than 1.5%. The maximum error (4.2%) appears in the small discharge region. The errors in the hump region also show much larger than other normal operating points around 2%. Also, from the efficiency-discharge curve the relative errors are much larger in the small discharge region and hump region. An obvious hump region could also be observed in efficiency-discharge curve. Nevertheless, the tendency of the numerical results is the same with the experimental data. All of the errors for the head, torque and efficiency, except the small discharge points, are less than 2%. It can be concluded that the results obtained through the numerical simulations are in a good agreement with the experimental data. Further study could be conducted based on the simulations.

## 4. Analysis of numerical results based on the vorticity dynamics theory

### 4.1 Unsteady analysis for vorticity dynamic parameters

According to Sec. 2, the total force interaction between the blades and the fluid comes from skin friction ($vor_1$) and surface normal pressure ($vor_2$) based on the vorticity dynamics theory. Hump region point ($0.72Q_{BEP}$) at the 19 mm guide vane opening was chosen to get the variation of the vorticity dynamic parameters over one period. Vorticity dynamic parameters skin friction and surface normal pressure distribution were obtained in the post-processing of commercial code ANSYS CFX 14.0 according to the vorticity dynamic parameters defined in Sec. 2. Fig. 7 shows the variation of the skin friction in the runner and guide vanes during the hump region over one period. In one period, the fluctuation of the maximum value at every moment is small, and the distribution changes little (see Fig. 7). The skin friction shows much higher on the pressure surfaces of the blades near the trailing edges and suction surfaces near the leading edges in the runner. Moreover, it appears obviously higher in the four guide vanes than the one from other guide vanes. This is due to these four guide vanes being close to special stay vane, so the flow is much more unstable. The distribution of the surface normal pressure is shown in Fig. 8. The value is obviously larger than the skin friction. In the whole period, the high value areas mainly happen at the leading edges and trailing edges of the blades and vanes. Only small change for the amplitudes and distribution area could be observed over the whole period.

Figs. 9 and 10 indicate the distribution of the skin friction work and surface normal pressure work. The distribution law of the skin friction work is the same with skin friction. The skin friction work in the guide vanes close to special stay vane is much higher than the one from other three guide vanes, especially near the top cover of the guide vanes. Furthermore, it is mainly focused on the trailing edges and a small area of leading edges near the hub on the pressure surfaces of the blades, while it is mainly located on the trailing edges near the band on the suction surfaces of the blades. In addition, the high value region has a larger distribution range on the suction surfaces than that on the pressure surfaces. As the same with the surface normal pressure, the surface normal pressure work at the trailing edges of the blades and leading edges of guide vanes shows much larger with only a small area. High value regions are mainly distributed in a concentrated area at the trailing edges on the pressure surfaces of the blades and near the bottom cover on the suction surfaces of guide vanes.

### 4.2 Hump characteristics analysis

Since, the fluctuations of the amplitude and distribution change little. For points $0.56Q_{BEP}$, $0.72Q_{BEP}$, $1.00Q_{BEP}$ and $1.34Q_{BEP}$ in the head-discharge curve, the final moment of the

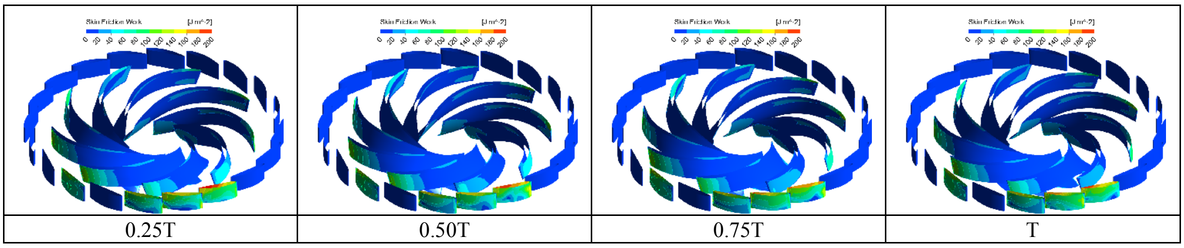

Fig. 9. The distribution of skin friction work over one period.

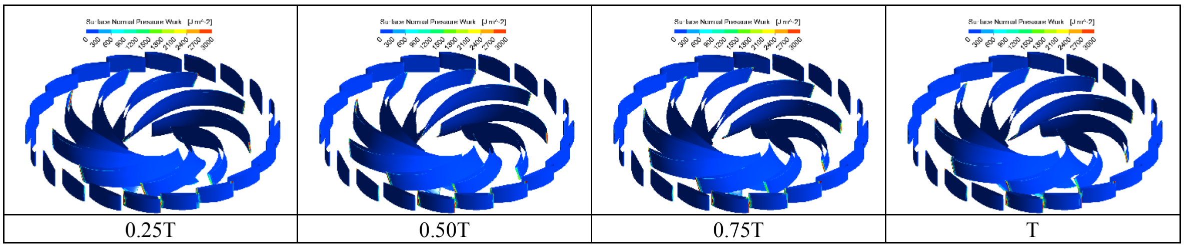

Fig. 10. The distribution of surface normal pressure work over one period.

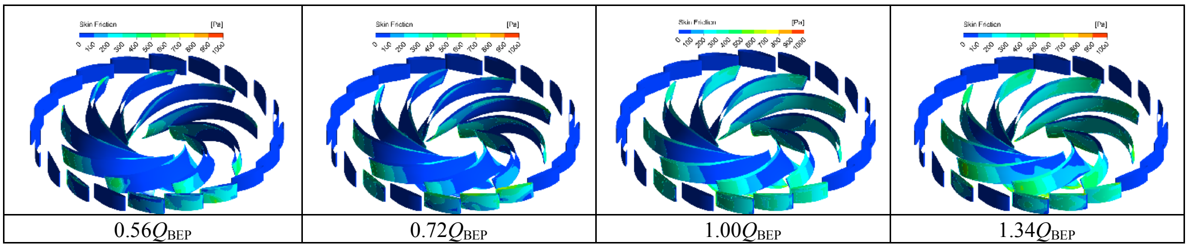

Fig. 11. Skin friction distribution with different operating conditions.

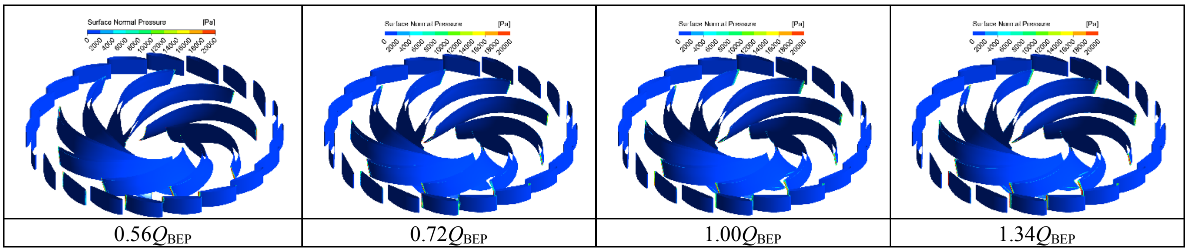

Fig. 12. Surface normal pressure distribution with different operating conditions.

last period was chosen to find the reasons of hump characteristics. From Fig. 11, it could be noticed that the high value regions of the skin friction work decrease as the discharge is reduced. However, the values in the guide vanes near the special stay vane at the point 0.72$Q_{BEP}$ show a bit larger than those from other operating points. It indicates that the losses induced by the skin friction in the guide vanes in the hump region are larger. With respect to the surface normal pressure (see Fig. 12), the law of the distribution is almost the same for four operating points. The distribution is uniform from the leading edge to the trailing edge along the blade direction. Only some small high value regions at the leading edges and trailing edges of the blades can be found, and the values for these regions decrease with the reduction of the discharge.

The skin friction work and surface normal pressure work for different operating conditions are shown in Figs. 13 and 14. It can be clearly observed that the skin friction work in the guide vanes is much larger. The area integrals of the skin friction in the runner are 6.07J, 6.87J, 10.67J and 14.87J for 0.56$Q_{BEP}$, 0.72$Q_{BEP}$, 1.00$Q_{BEP}$ and 1.34$Q_{BEP}$, respectively. In the stay-guide vanes, the values for these four points are, respectively, 8.89J, 12.59J, 15.9J and 19.21J. As for the surface normal pressure work, the area integrals in the runner (the energy comes from the rotating runner) are 33.38J, 33.31J, 40.75J and 53.45J, respectively. It can be concluded that the hump characteristics are related to the reduction of the surface normal pressure work in the runner and the increase of skin friction work in the stay-guide vanes.

The streamlines in the runner and stay-guide vanes under different operating conditions are shown in Fig. 15. Several

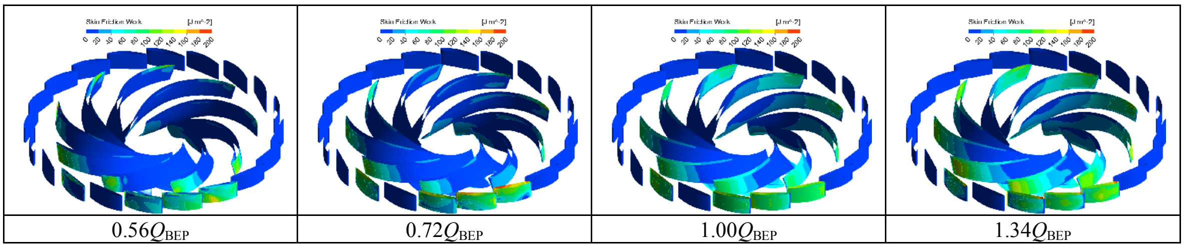

$0.56Q_{BEP}$ $0.72Q_{BEP}$ $1.00Q_{BEP}$ $1.34Q_{BEP}$

Fig. 13. Skin friction work distribution with different operating conditions.

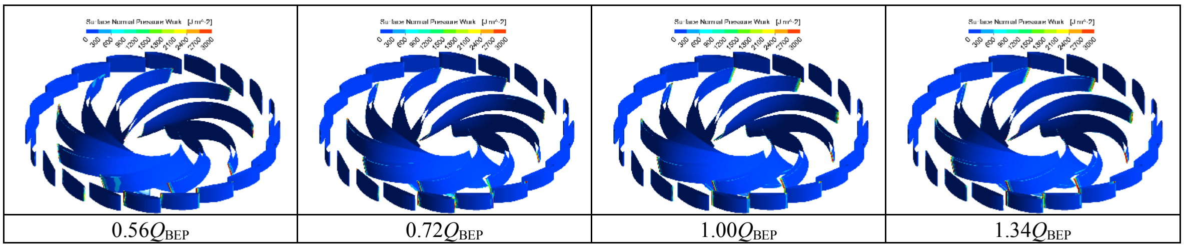

$0.56Q_{BEP}$ $0.72Q_{BEP}$ $1.00Q_{BEP}$ $1.34Q_{BEP}$

Fig. 14. Surface normal pressure work distribution with different operating conditions.

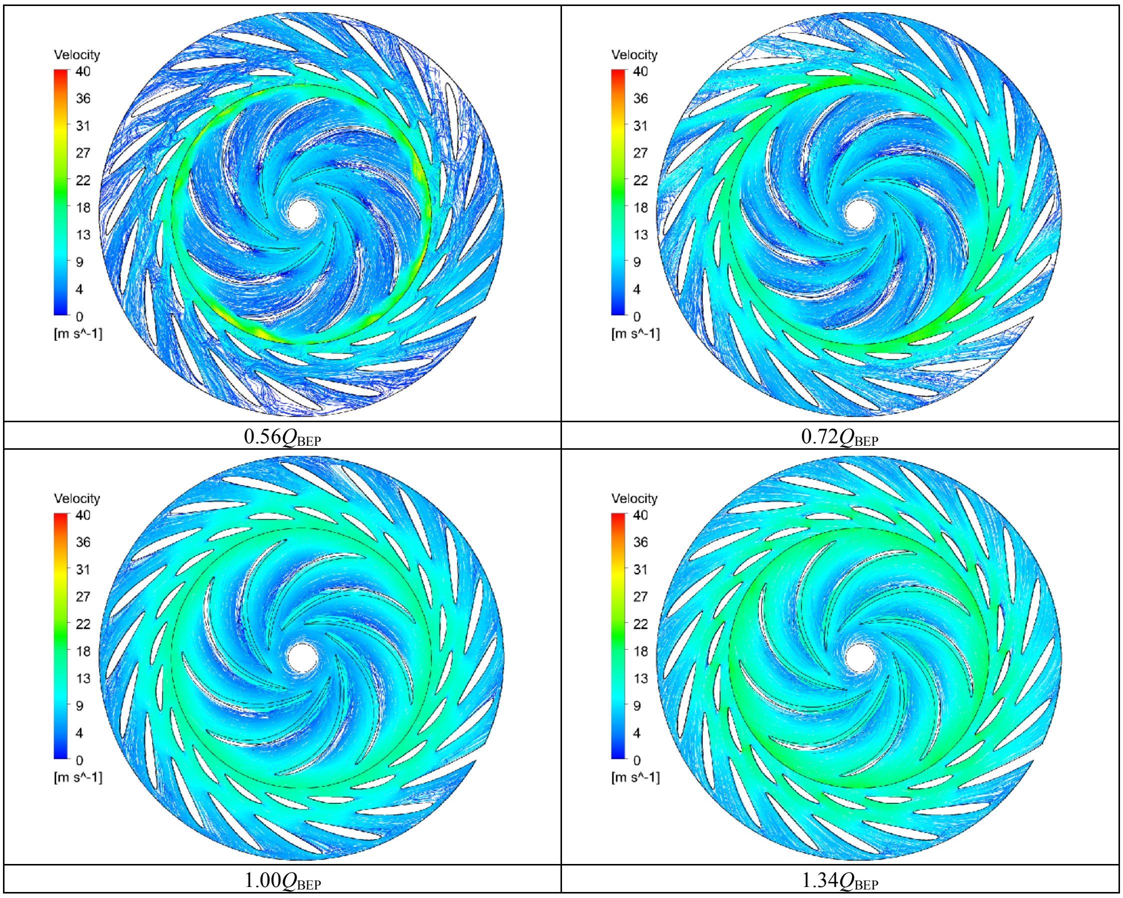

$0.56Q_{BEP}$ $0.72Q_{BEP}$

$1.00Q_{BEP}$ $1.34Q_{BEP}$

Fig. 15. Streamlines in the runner and stay-guide vanes for different operating conditions.

obvious vortices can be observed under different operating conditions. In the passages of the stay vanes close to special stay vane, the flow is unstable and flow separation appears for these four operating points. Obvious flow separation on the suction surfaces near the trailing edges could be also observed, which corresponds with the skin friction work.

To validate that the vortex and flow separation comes from the skin friction work, Q-criterion was chosen to show the vortex in the runner and stay-guide vanes. The value was set as $2.0\times10^{6}$ $s^{-2}$ (see Fig. 16). It is easy to find that the distriution

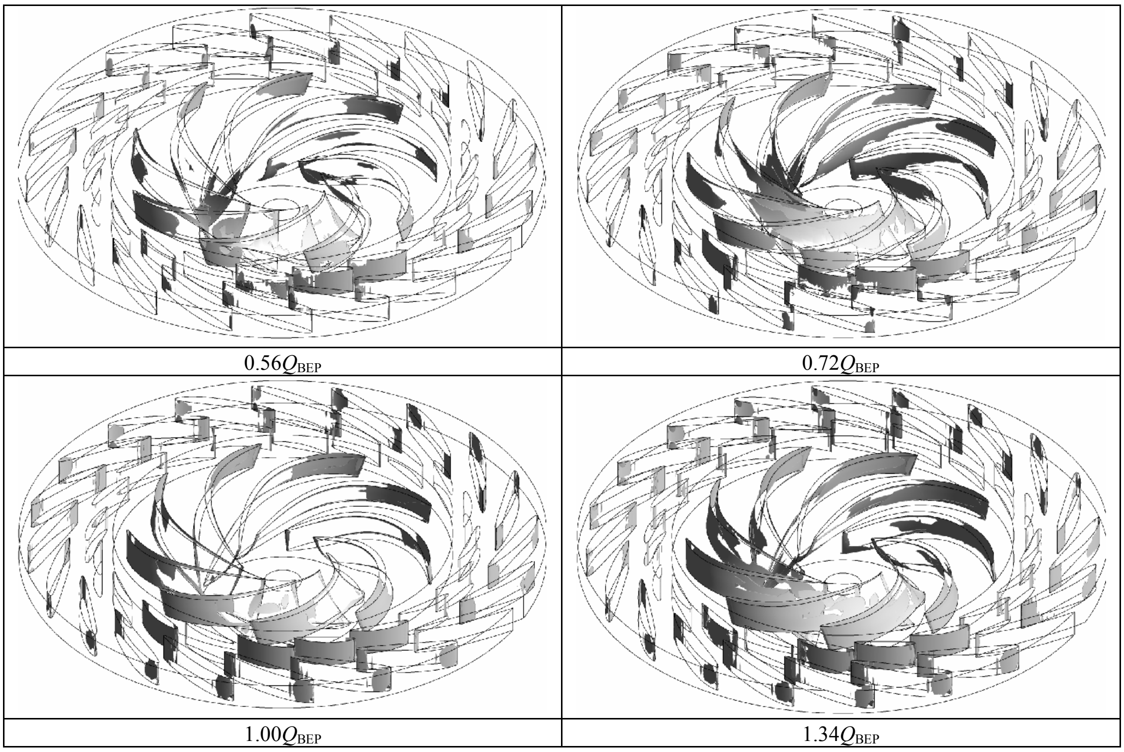

$0.56Q_{\mathrm{BEP}}$ $0.72Q_{\mathrm{BEP}}$

$1.00Q_{\mathrm{BEP}}$ $1.34Q_{\mathrm{BEP}}$

Fig. 16. Vortex core region for different operating conditions.

law of the voxtex core is the same with the skin friciton work. It mainly occurs in the leading edges on the suction surfaces and trailing edges on the pressure surfaces of the blades under different operating conditions. The four guide vanes close to the special stay vane show an much more obvious vortex core. As the dischage is reduced, the vortex core regions turn out to decline near trailing edges on the suction surfaces in the runner. However, it shows much larger on the suction surfaces close to leading egdes of the blades for the hump region point $0.72Q_{\mathrm{BEP}}$. It is the same distribution law of the vortex core with the skin friction work.

It can be concluded that vortex generation is mainly produced by the skin friction work. As a result, hump characteristics are related to the reduction of the surface normal pressure work and vortex motion on the suction surfaces close to the leading edges in the runner, and the increase of skin friction work in the stay-guide vanes. As for a Francis pump turbine, blade features long in the radial direction, and the vorticity parameters are distributed non-uniformly on the blades. The surface normal pressure work that blades act on the fluid shows higher on the blade trailing edges, and the skin friction is mainly concentrated on leading and trailing edges of the blades. In other words, the blade leading and trailing edges are the most obvious positions for the blades acting on the fluid.

## 5. Conclusions

We performed 3-D unsteady flow simulations in a full pump turbine model using the SST $k$-$\omega$ turbulence model. The dynamic mechanism between the runner and the fluid under different operating conditions was analyzed based on the theory of vorticity dynamics. The results indicate that the theory of vorticity dynamics has advantages in evaluating the dynamic performance of a pump turbine model.

(1) Based on the vorticity dynamics theory, the energy transfer between the runner and the fluid is through vorticity dynamic parameters-pressure (surface normal pressure) and friction terms (skin friction), and the surface normal pressure term accounts for the most.

(2) Through the analysis of vortex based on the vorticity dynamic parameters, vortex generation is mainly produced by the skin friction work.

(3) Using vorticity dynamic analysis combined with the method of Q-criterion, it can be concluded that hump characteristics are related to the reduction of the surface normal pressure work and vortex motion on the suction surfaces close to the leading edges in the runner, and the increase of skin friction work in the stay-guide vanes.

The analysis using vorticity dynamics theory shows the vortex comes from the skin friction on the blade surfaces. The exact position where the skin friction distributes could be detected. The blade shape could be modified according to the distribution of the skin friction. Further study should be continued based on the above studies. More investigation should be carried out to validate the relation between hump characteristics and skin friction. Their quantitative relationship is still unclear. More attention should focus on the mechanism of the skin friction leading to the flow separation and vortex.

## Acknowledgment

This work was supported by Foundation for Innovative Research Groups of the National Natural Science Foundation of China (Grant No. 51121004) and China Scholarship Council (CSC) (Grant No.201506120168).

## Nomenclature

$Q_{BEP}$ : Discharge of best efficiency point
$\vec{v}$ : Flow velocity
$\rho$ : Density
$p$ : Pressure
$\mu$ : Dynamic viscosity of the fluid
$\vec{f}$ : A conservative external body force
$\vec{\omega}$ : Vorticity field
$\vec{b}$ : Any vector specified
$S$ : Control surface
$\vec{n}$ : Normal direction of the control surface
$V_f$ : Control volume
$vor_1$ : Skin friction
$vor_2$ : Surface normal pressure
$vor_3$ : Skin friction work
$vor_4$ : Surface normal pressure work
$n_q$ : Specific speed of the pump-turbine in pump mode, $n_q = \frac{n\sqrt{Q}}{H^{3/4}}$, (m, m$^3$/s)

## References

[1] Ch. Gentner, Z. Smiljcic and M. Sallaberger, Analysis of unstable pump characteristics of pump turbines, *16th Intern. Seminar on Hydropower Plants-Reliable Hydropower for a Safe and Sustainable Power Production,* Vienna (2010).

[2] O. Braun, J. L. Kueny and F. Avella, Numerical analysis of flow phenomena related to the unstable energy-discharge characteristic of a pump-turbine in pump mode, *Proceedings of 2005 ASME Fluids Engineering Division Summer Meeting and Exhibition,* Houston, USA (2005).

[3] J. T. Liu, S. H. Liu and Y. L. Wu, Numerical investigation of the hump characteristic of a pump-turbine based on an improved cavitation model, *Computer and Fluids,* 68 (2012) 105-111.

[4] J. Yang, G. Pravesi and S. Yuan, Experimental characterization of a pump - Turbine in pump mode at hump instability region, *J. of Fluids Engineering*, 137 (051109) (2015) 1-11.

[5] H. J. Ran, X. W. Luo and L. Zhu, Experimental study of the pressure fluctuations in a pump turbine at large partial flow conditions, *Chinese J. of Mechanical Engineering*, 25 (6) (2012) 1205-1209.

[6] J. Yan, J. Koutnik and U. Seidel, Compressible simulation of rotor-stator interaction in pump-turbines, *Proceedings of 25th IAHR Symposium on Hydraulic Machinery and Systems,* Timisoara, Romania (2010).

[7] R. Z. Gong, H. J. Wang, L. X. Chen and D. Y. Li, Application of entropy production theory to hydro-turbine hydraulic analysis, *Sci. China Tech. Sci.*, 56 (7) (2013) 1636-16437.

[8] D. Y. Li, R. Z. Gong and H. J. Wang, Dynamic analysis on pressure fluctuation in vaneless region of a pump turbine, *Sci. China Tech. Sci.*, 58 (5) (2015) 813-824.

[9] D. Y. Li, R. Z. Gong and H. J. Wang, Unsteady simulation and analysis for hump characteristics of a pump turbine model, *Renew Energ.*, 77 (2015) 32-42.

[10] X. J. Wu, Unsteady flow simulation and vortex flow diagnosis of a Francis turbine, *Ph.D. Thesis*, Beijing, Tsinghua University (2009).

[11] J. Z. Wu, R.W. Tramel and F. L. Zhu, A vorticity dynamics theory of three-dimensional flow separation, *Phys. Fluids*, 12 (8) (2000) 1932-1954.

[12] Y. T. Yang, H. Wu and Q. S. Li, Vorticity dynamics in axial compressor flow diagnosis and design, *ASME J. Fluids Eng.*, 130 (041102) (2008).

[13] R. K. Zhang, V. Dam and J. Z. Wu, Aerodynamic characteristics of wind turbine blades with a sinusoidal leading edge, *Wind Energy*, 15 (3) (2012) 407-424.

[14] A. Surana, G. B. Jacons and O. Grunberg, An exact theory of three-dimensional fixed separation in unsteady flows, *Phys. Fluids*, 20 (10) (2008) 107101.

[15] F. C. Li, H. G. Fan and Z. W. Wang, Coupled design and optimization for runner blades of a tubular turbine based on the boundary vorticity dynamics theory, *ASME-JSME-KSME 2011 Joint Fluids Engineering Conference*, 1 (2010) 603-609.

[16] L. Zhang, S. H. Liu and Y. L. Wu, Vorticity dynamics analysis on flow in Francis hydraulic turbine, *ASME 2006 2nd Joint U.S.-European Fluids Engineering Summer Meeting Collocated with the 14th International Conference on Nuclear Engineering,* Miami, Florida, USA (2006) 21-725.

[17] J. Z. Wu, *An introduction to vorticity dynamics,* Higher Education Press (1993) (in Chinese).

[18] J. C. Wu, *Elements of vorticity aerodynamics*, Springer (2005).

[19] Q. S. Li, H. Wu and M. Guo, Vorticity dynamics in axial compressor flow diagnosis and design—Part II: Methodology and application of boundary vorticity flux, *ASME J. Fluids Eng.*, 132 (1) (2009) 011102.

[20] D. Y. Li, R. Z. Gong and H. J. Wang, Numerical investigation in the vaned distributor under different guide vanes openings of a pump turbine in pump mode, *J. of Applied Fluid Mechanics,* 9 (1) (2016) 253-266.

[21] IEC60193, *Hydraulic turbines, storage pumps and pump turbines-model acceptance tests* (1999) 107-108.

**Deyou Li** is currently a Ph.D. candidate at School of Energy Science and Engineering, Harbin Institute of Technology, China. He received his B.S. and M.S. from Harbin Institute of Technology, in 2010 and 2012, respectively. His research interests include numerical simulation and experimental investigation of a pump turbine, turbine and pump.